

The Balloon Experimental Twin Telescope for Infrared Interferometry (BETTII): towards the first flight

Maxime J. Rizzo^a, S. A. Rinehart^b, A. Dhabal^a, P. Ade^c, D. J. Benford^b, D. J. Fixsen^b,
M. Griffin^c, R. Juanola-Parramon^e, D. T. Leisawitz^b, S. F. Maher^b, E. Mentzell^b,
L. G. Mundy^a, A. Papageorgiou^c, E. Pascale^c, R. F. Silverberg^b, G. Savini^f, J. Staguhn^d,
T. J. Veach^e, and J. Vila Hernandez de Lorenzo^g

^aUniversity of Maryland, College Park, MD 20721

^bNASA Goddard Space Flight Center, Greenbelt, MD 20771

^cCardiff University, Cardiff, UK

^dJohns Hopkins University, Baltimore, MD 21218

^eOak Ridge Associated Universities, NASA Postdoctoral Program Fellow

^fUniversity College, London, UK

^gCatholic University of America, Washington, DC

ABSTRACT

The Balloon Experimental Twin Telescope for Infrared Interferometry (BETTII) is a balloon-borne, far-infrared direct detection interferometer with a baseline of 8 m and two collectors of 50 cm. It is designed to study galactic clustered star formation by providing spatially-resolved spectroscopy of nearby star clusters. It is being assembled and tested at NASA Goddard Space Flight Center for a first flight in Fall 2016. We report on recent progress concerning the pointing control system and discuss the overall status of the project as it gets ready for its commissioning flight.

Keywords: BETTII, interferometry, balloon, far-infrared, star formation

1. INTRODUCTION

The BETTII payload is an 8 m fixed-baseline interferometer, equipped with two 50 cm siderostats. It operates in two wavelength bands, 30–55 μm and 55–110 μm (subsequently referred to as Band 1 and 2 respectively). In these two bands, its theoretical angular resolution is $\sim 0.5''$ and $\sim 1''$, respectively. This is significantly better than all existing or previous facilities that operate in the far-infrared, which have traditionally been limited by the mirror size. In addition, this matches the resolution of JWST at 25 μm , hence providing a good continuity to probe astrophysical phenomena at longer wavelength but with the same linear resolution. BETTII will fly on a stratospheric balloon up to 120 000 ft to observe the far-infrared (far-IR) universe at high angular resolution. Its first flight is scheduled for September 2016.

There are four major components to BETTII: the mechanical structure;¹ the optics (Dhabal et al., these proceedings); the cryostat and the detectors;² and the control system,³ on which we give updates in this paper. Fig. 1 shows a CAD rendering of the BETTII payload with the key elements of the instrument, while Fig. 2 shows the payload in the high bay at NASA Goddard in July 2016. The distance between the left and right siderostats is ~ 8 m.

This paper focuses on recent data showing the performance of BETTII's pointing control system. BETTII has an alt/az pointing strategy: reaction wheels are used to control the payload in azimuth, while rotation stages are used to control the siderostats in elevation. The pointing control system is organized in two loops: a coarse loop, which aims to bring the siderostats within $\pm 15''$ of a guide star near the target; and a fine loop which acquires a near-IR image of the guide star from each arm, and ensures overlap of the beams in the science channels. Once the observatory is pointing to the target and the two beams are overlapped at the science detectors, a final

Send correspondence to Dr. Rinehart at stephen.a.rinehart@nasa.gov

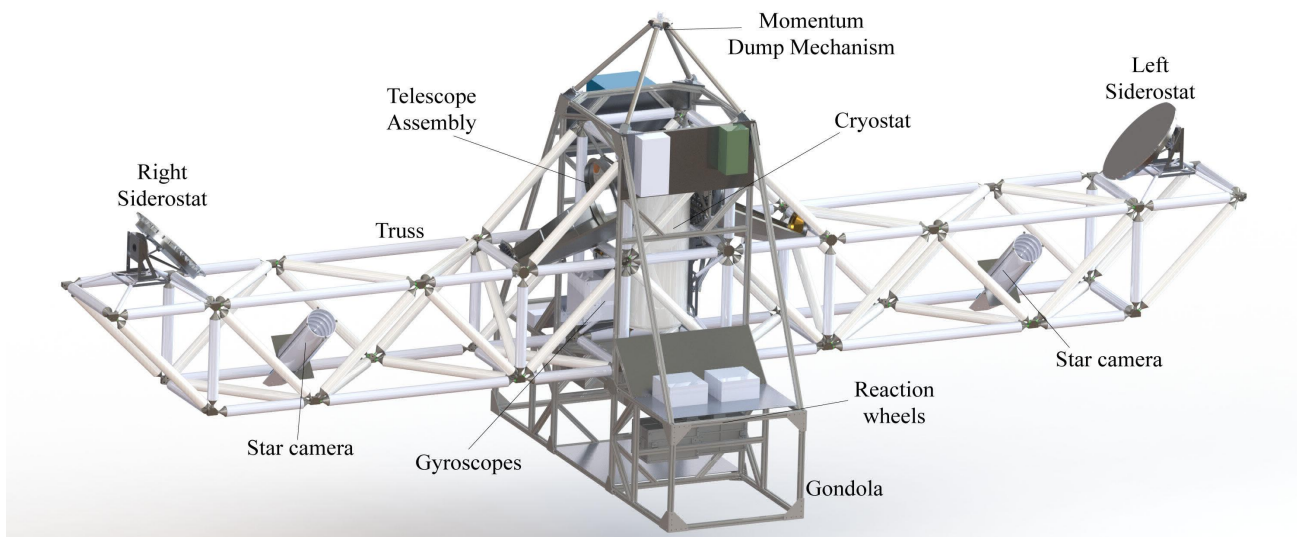


Figure 1: CAD rendering of the BETTII payload.



Figure 2: Payload hanging in the high bay in early July 2016. The control system and electronics are assembled. The only part of the system missing is the cryostat which contains the science detectors and the guide camera.

control loop is used: the phase loop, which aims at correcting errors in the optical path difference introduced by attitude errors using a delay line linear mechanism.

In the following, we show results from our gyroscope and star camera characterization, as well as on-sky results of the coarse pointing loop which was tested extensively in the Spring of 2016.

2. SENSOR CHARACTERIZATION

The two main sensors that we discuss here are our gyroscopes and our star cameras, which are used together to estimate our orientation (or *attitude*) in the inertial reference frame.

2.1 Gyroscopes

We purchased three SRS-2000 fiber-optic gyroscopes from Optolink. This gyroscope technology uses the Sagnac effect and is the cutting edge in inertial rotational velocity measurements.⁴ We chose these devices for their low angular random walk, which is a measure of their inherent noise.

The devices have a bandwidth of 50 Hz, but can be triggered at up to 2000 Hz. Their extreme stability is contingent upon proper temperature stabilization, which is done with a closed loop set at their calibration temperature of $23.5^{\circ}\text{C} \pm 0.5^{\circ}\text{C}$ using an active built-in Peltier element. This Peltier element transforms electric power into either heating or cooling.⁵

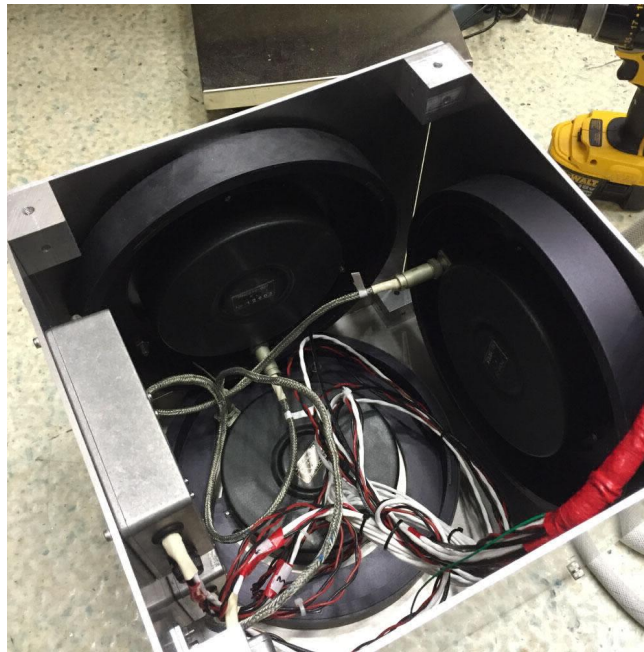


Figure 3: Three single-axis Fiber Optic Gyroscopes are mounted in an orthogonal assembly and attached to the truss.

The three single-axis gyroscopes are assembled in an orthogonal mount configuration shown in Fig. 3. In the following, we describe how we measure the various properties of the gyroscopes, and discuss how they compare to the specifications. The gyroscopes' sensitivity has complicated some of their testing. As soon as we attach a gyroscope to any structure, it measures its vibrational modes, which makes it difficult to make a stable measurement of the gyroscope's drift stability. This includes the vibrations that are inherent to the building in which they are placed.

We were successful at measuring the gyroscope properties over long periods of time by attaching them flush to a heavy slab of metal, and putting the slab of metal flush on the vibration-isolating floor of one of NASA Goddard's optics labs in building 34.

We proceeded to an identical series of tests for each gyroscope:

1. We acquired data at 2000 Hz for 10 min to measure a proper power spectral density and characterize the noise;
2. We acquired data at 100 Hz for ~ 8 h to study the drift properties.

The properties that we are looking for are typical instantaneous angular random walk, and the overall drift instability of the gyroscope's mean. When the gyroscopes are set on the floor, they measure a component of the Earth's rotation vector in inertial space. The mean of the measurement depends on the exact angle at which the device is placed with respect to the zenith vector, and is of no importance for this noise study. We seek to understand how much the mean varies over long periods of time. To minimize disturbances from the building vibrations (opening/closing of doors, etc), we operated entirely after regular working hours.

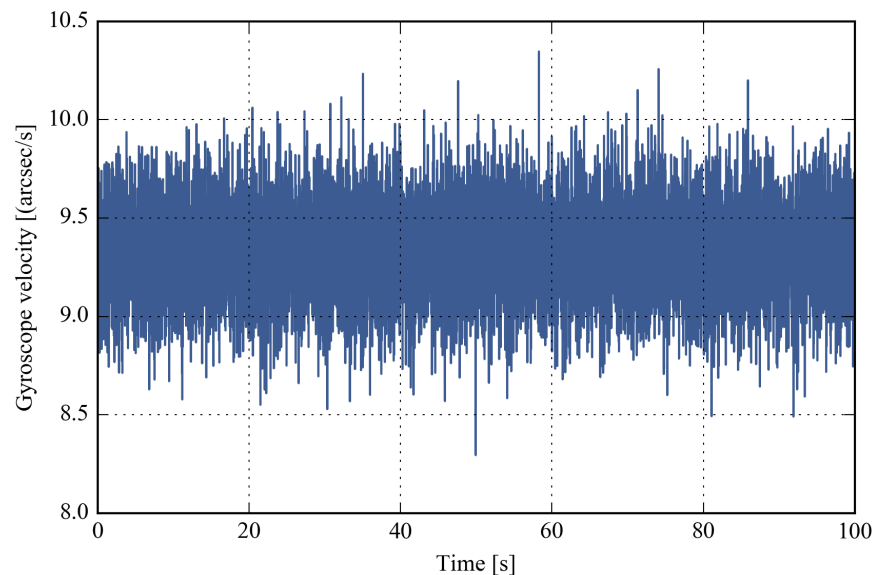


Figure 4: Snapshot of 100 s of gyroscope data, taken from our 8 h data sample.

The angular random walk (ARW) is a measure of the effects of integrating a noisy velocity measurement. The specification from the manufacturer is $\text{ARW} = 5 \times 10^{-4} \text{ deg h}^{-0.5}$. This means that if we integrate the gyroscope's rate for 1 hour, the 1σ uncertainty on our position would be $5 \times 10^{-4} \text{ deg} \sim 1.8''$. For an integration time of 1 second, it would be $0.03''$. For a single integration time step $\Delta t = 10 \text{ ms}$, it would be $0.003''$.

The manufacturer specification gives a maximum bias instability over a wide range of temperatures less than 0.005 deg h^{-1} . This represents how much the mean angular velocity is expected to vary. These tests are an attempt to verify these numbers.

2.1.1 Power spectral density

The usual frequency-domain analysis tool is the power spectral density (PSD). This allows us to spot any frequency peaks in the data, and let us look at the $1/f$ noise behavior, which is the typical low-frequency behavior that indicates drifts in the signal. The 100 Hz data is all we need, as the gyroscope's bandwidth is 50 Hz. Hence, the 2000 Hz data does not contain any more information than the 100 Hz. In fact, while plotting the PSD of the 2000 Hz data, we can see clearly the break at 50 Hz characteristic of a 50 Hz low-pass filter.

It is important to note that in their factory settings, the gyroscopes' noise distribution was not normal at all. It exhibited electronic peaks with many harmonics, at frequencies that were varying as a function of the gyroscope inclination (as it was measuring different components of the Earth's rotation). After talking to the manufacturer, we determined that it was caused by the closed-loop algorithms inside the gyroscope electronics. The problem was known by them, and the remedy was to inject a random phase perturbation in the closed loop.

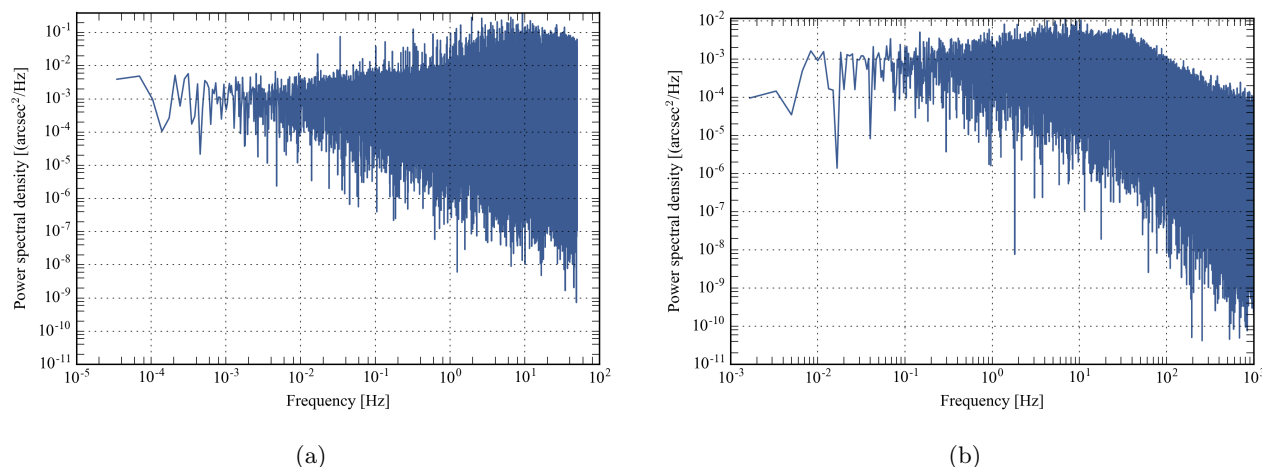


Figure 5: (a): Single-sided power spectral density for gyro 11005, an 8 h sample with a sampling rate of 100 Hz, showing no particular feature (large peaks or resonances). (b): Single-sided power spectral density for gyro 11005, a 10 min sample with a sampling rate of 2000 Hz, showing no electronic resonance peak or other feature. We can notice the -3 dB break at around 50 Hz.

This had the effect of getting rid of those frequency peaks, at the cost of increasing the overall noise variance by a factor of 4. The noise levels that are specified by the company are very close to the noise seen when using that random phase modulation. Hence, if one does not care as much at the frequency content of the gyroscope, it is possible that this device could work even much better than it does for us.

2.1.2 Normality tests

We ran a few standard normality tests on chunks of the 8-hour data for each gyroscope. While the tests on individual small chunks of data never reject the null hypothesis (that the distribution is normal), the distribution of the total 8 hours does with a very high probability, using both the Anderson-Darling and the Kolmogorov-Smirnov test. It means that it is extremely unlikely that the measured noise over 8 h is coming from a normal distribution.

However, since the data is always consistent with being normally distributed over timescales of tens of minutes, after close inspection of the long-term quartile plots and histograms, we determined that it would be safe to consider the distribution as normal for the purpose of our attitude estimator (see Fig. 6).

2.1.3 Allan variance

Another common tool to study of the gyroscope's performance is to plot the Allan variance. The Allan variance gives a time-domain analysis of the gyroscope's noise that is complementary to the power spectral density, by plotting the variance (or standard deviation) between the means of clusters of data over various lengths. On the Allan deviation plots shown for our gyroscopes in Fig. 7, the angular random walk (ARW) can be measured as the deviation at 1 s cluster interval, and the bias drift measured as the deviation for 10 000 s cluster interval.

2.1.4 Gyros in flight configuration

Fig. 8 show the power spectral density of the gyroscopes in their flight configuration, mounted on BETTII's carbon fiber truss structure. The left column shows the PSD of the three gyroscopes on a log-log plot, and the right panel shows the PSD on a linear-linear plot, zoomed in on the tallest peaks. These three peaks are attributed to the carbon fiber truss first resonant frequencies, which were expected to be around 25 Hz. The lower peaks at a few hertz are attributed to the passive vibration dampers that connect the truss to the gondola.

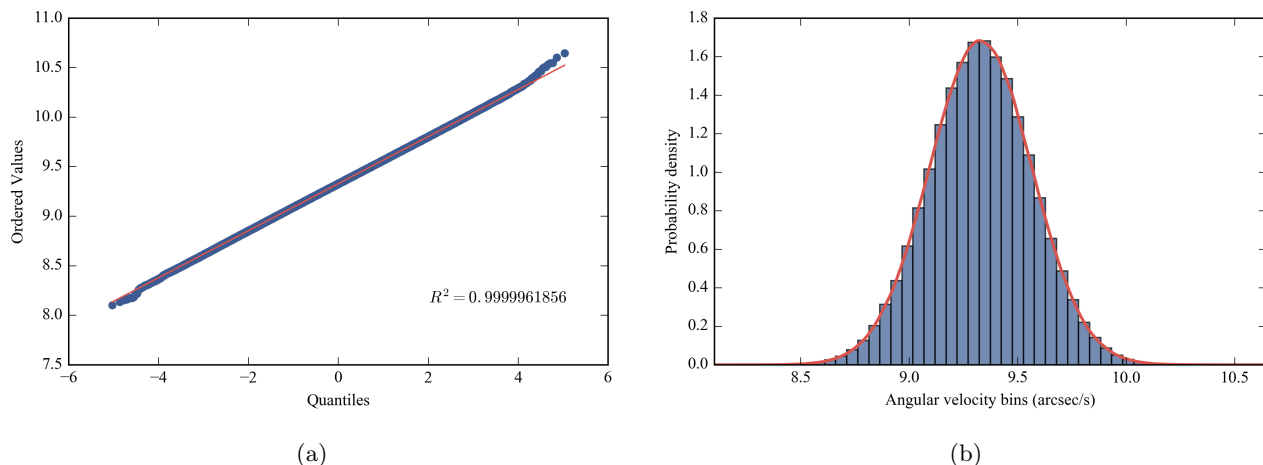
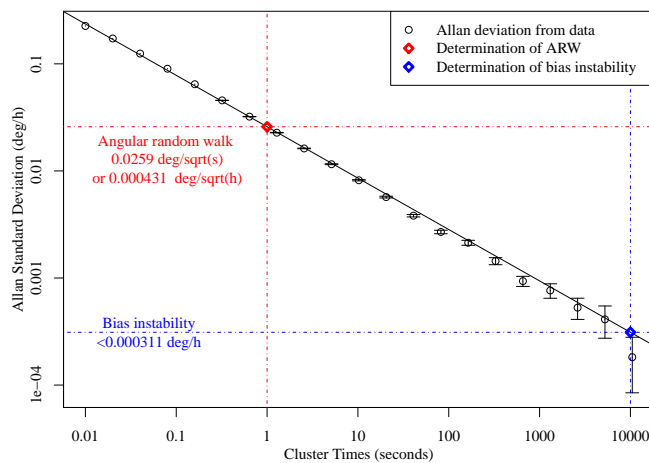


Figure 6: Normality analysis of the gyroscope signal over 8 h of data taken at 100 Hz. (a): Normal quantile-quantile plot for an 8 h sample with a sampling rate at 100 Hz. Here the measured quantiles (fraction of the measured values under a certain value) are plotted against the theoretical quantiles from a normal distribution. The red line is the theoretical distribution if the data were taken from a normal distribution. (b): Probability density distribution for an 8 h sample with a sampling rate at 100 Hz. In red, the theoretical normal distribution we obtain with the measured mean and standard deviation from the sample. While the data is not strictly normally distributed, we consider that it is sufficiently close to a gaussian distribution.

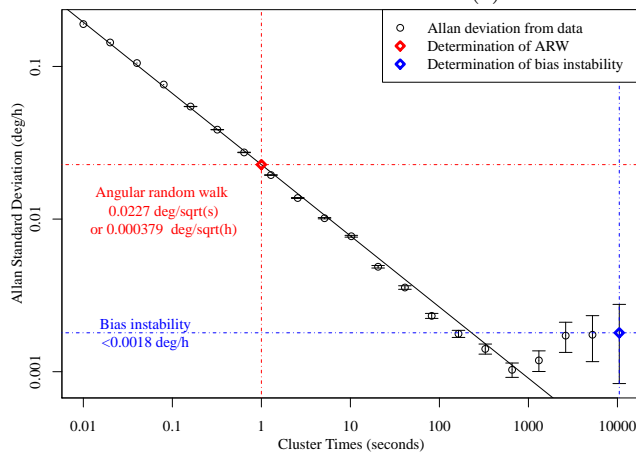
Table 1: Gyroscope properties

Measured property	Gyro #11005	Gyro #12003	Gyro #12004
Standard deviation (deg h^{-1})	0.237	0.199	0.217
Angular random walk ($\text{deg h}^{-0.5}$)	4.31×10^{-4}	3.79×10^{-4}	4.02×10^{-4}
Bias instability (deg h^{-1})	3.11×10^{-4}	1.8×10^{-3}	3.05×10^{-4}

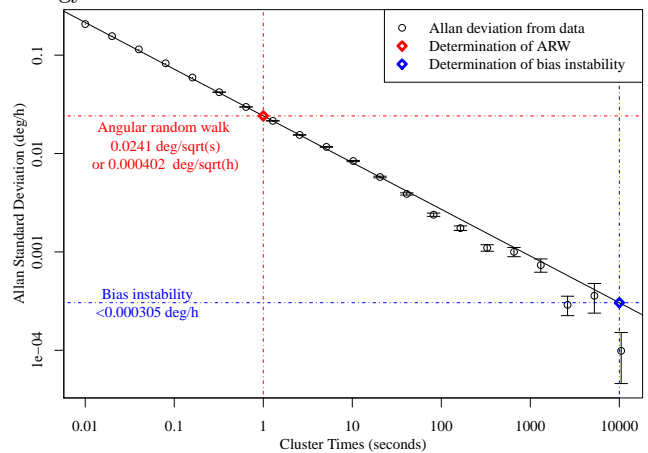
Notes: Properties of the gyroscopes determined from the Allan variance analysis on an 8 h sample with a sampling rate at 100 Hz. Note that $1 \text{ deg h}^{-1} = 1 \text{ arcsec s}^{-1}$, and the Earth rotates at about 15 arcsec s^{-1} about the line joining the two poles.



(a) Allan deviation of gyro 11005

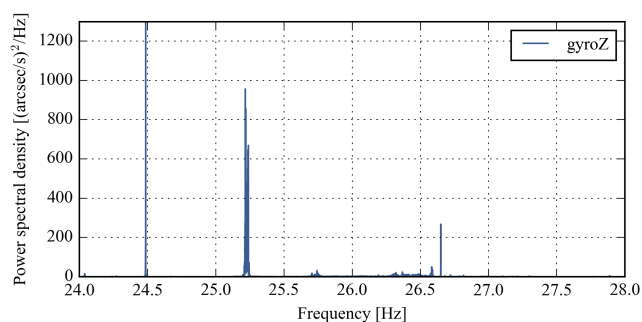
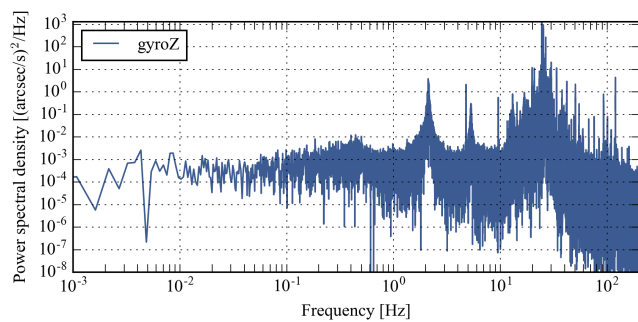
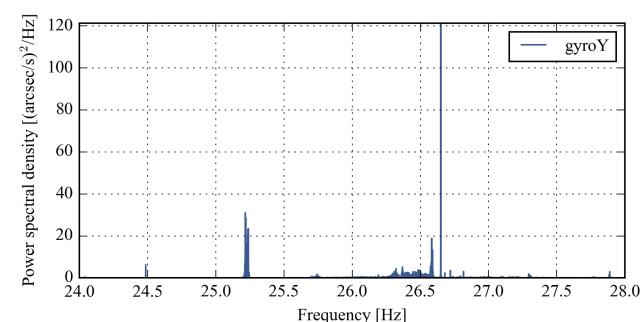
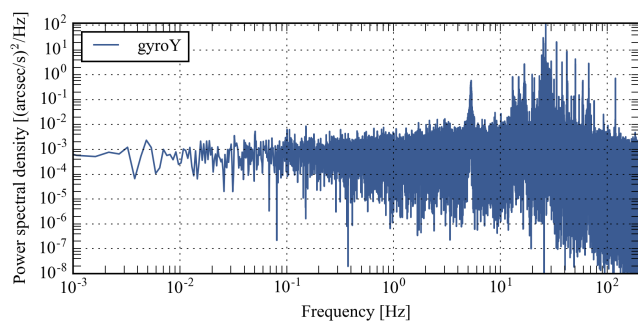
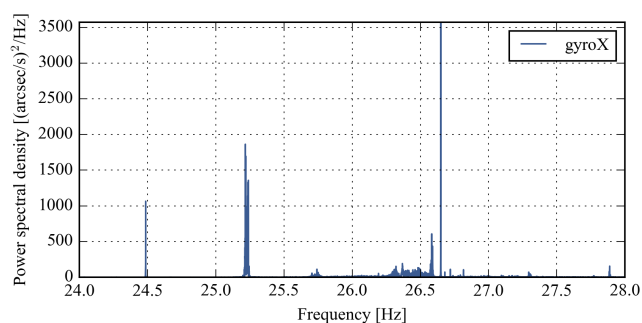
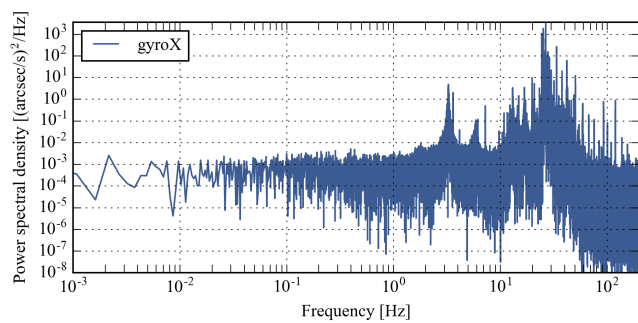


(b) Allan deviation of gyro 12003



(c) Allan deviation of gyro 12004

Figure 7: Allan deviation plots. The red lines indicates show the extracted value for angular random walk, while the blue lines show the extracted values for the bias instability.



(a)

(b)

Figure 8: Gyroscope noise measurements (a) Power spectral density in log-log plot (b) Power spectral density in linear-linear

2.2 Star cameras

2.2.1 Design

We have designed, built and tested a custom star camera setup that provides higher accuracy measurements than commercially available devices for a much lower cost. An image of our assembly is shown in Fig. 9. Our collaborators from Cardiff University provided the star camera software, which solves for the inertial orientation from a given picture. This software is a C++ set of routines that was originally developed for the EBEX balloon experiment.⁶

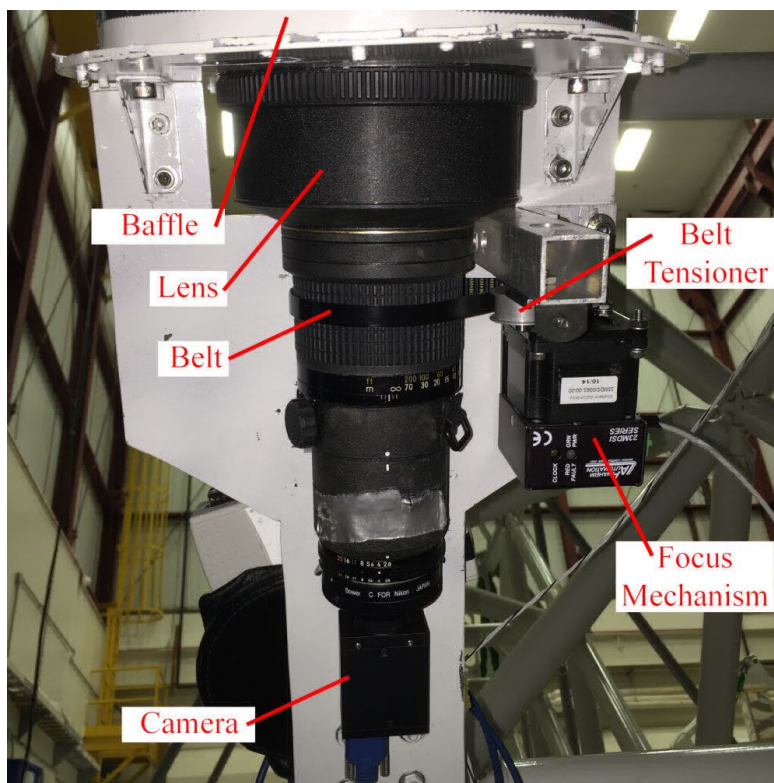


Figure 9: Star camera assembly featuring the lens, the camera, and the focusing system.

Our star camera design features a Nikon Nikkor 300 mm f/2.8 telefocal lens with manual focus and extended hood. These lenses were manufactured between 1977 and 1982 and can be found today online through websites like e-Bay. The lens provides low chromatic aberration, a magnification of $688''\text{mm}^{-1}$, a wide field of view ($\approx 10^\circ$) and a collecting area of 90cm^2 which is larger than most star tracking assemblies. This old lens does not feature a built-in autofocus or any of the image stabilization actuators commonly found in modern lens assemblies, which would have become a liability in the severe balloon environment.

Our camera is a USB3.0 Point Grey Grasshopper3. The sensor is a Sony Pregius IMX174 CMOS sensor with 1920×1200 pixels at $5.86\text{ }\mu\text{m}$ pitch. This provides a field of view of $2.14^\circ \times 1.34^\circ$ and a pixel scale of $4.02''/\text{pixel}$. It features a very convenient Linux-compatible software suite which works with all the Point Grey camera products, and leaves room for future potential upgrades of the camera. The detector characteristics are summarized in Table 2.

We have successfully cycled the camera in the environmental chamber all the way until the camera's internal thermometer indicated a temperature of -80°C , and it continued operating nominally.

2.2.2 Focusing strategy

Focusing the camera could be required at float due to the change in temperatures that could create a shift of the focal plane. We implemented our own autofocus mechanism: a belt is attached between the lens' focus ring

Table 2: Star camera properties

Property	Value	Description
Quantum efficiency at 525 nm (%)	76	Fraction of incoming photons that create signal
Read noise (electrons)	6.83	Error made when reading the pixel's value
Absolute sensitivity threshold (photons)	9.77	Minimum number of photons required to get a SNR = 1 on a pixel
Well depth (electrons)	32513	Maximum number of electrons a pixel can store

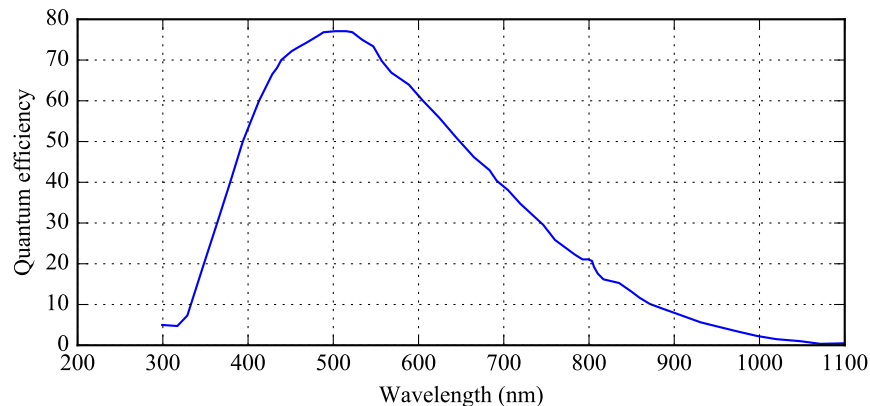


Figure 10: Quantum efficiency of star camera sensor.

and a stepper motor. When the stepper motor turns, it turns the focus ring. We tested this configuration in our environmental chamber only to realize that the belt was losing grip when the temperature was too cold. To fix this problem, we added a spring-based belt tensioner which adds ≈ 10 N of force to the belt.

At cold temperature and low pressure, we noted that the glass in the lens began to exhibit radial cracks, presumably caused by the coefficient of thermal expansion (CTE) difference between the steel housing and the glass material. These cracks do not noticeably affect image quality, but of course they could cause the glass to shatter if they become too large. Hence, it was decided to maintain the outside temperature of the lens above 0°C at all times during flight.

3. CONTROL LOOP IMPLEMENTATION AND TESTING

The flight software estimates the payload's attitude using a Multiplicative Extended Kalman filter (MEKF) to realize sensor fusion between the 100 Hz gyroscope measurements and the 0.5 Hz star camera measurements. The gyroscope model that is adopted introduces a bias in the measurement which is allowed to drift slowly with time. Using quaternions for our basic attitude representation, the Kalman filter can then fully represent the problem using 6 states: 3 for the vector part of the quaternion, and 3 for the velocity bias on each gyro.

This estimate is done completely in celestial coordinates as opposed to local coordinates so it does not fundamentally need time and geographic location. The coarse control is entirely done in the gyroscope reference frame, which is the relevant frame for both the azimuth actuators (the compensated controlled moment gyros, CCMG) and the elevation actuators.

An extensive discussion of the pointing control system strategy and design is offered in Rizzo et al. 2016 (Ph.D. thesis) and Rizzo et al. 2017 (in prep.). For completeness, we show in Fig. 11 the overall control diagram for the BETTII payload.

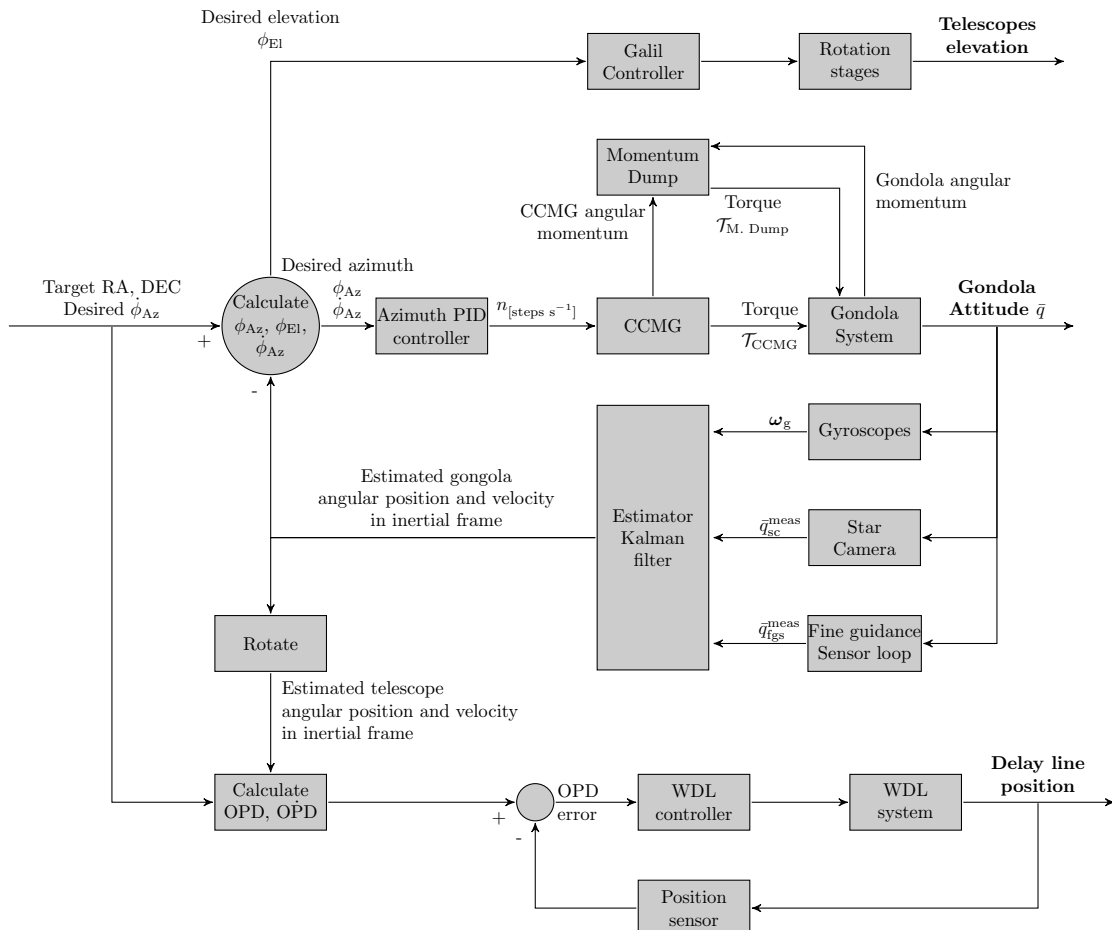


Figure 11: Control system architecture. The target RA, DEC, and desired azimuth velocity are the inputs to the control system. The payload controls azimuth and elevation separately, and the core of the software is the Kalman filter attitude estimator, which uses either the star camera measurements (coarse loop), or the measurements from the fine guiding sensor loop (fine loop). The phase loop is shown at the bottom of the diagram, where the Optical Path Difference (OPD) is corrected in a closed loop using a delay line.

Note that all controllers are using PID loops which feature a deadband parameter to avoid exciting high frequencies.

The flight software has a number of modes which are essential for the mission, such as tracking and slewing. All modes use the same fundamental software architecture, except that they can have different PID gains and various loops can be turned on or off. The slew mode uses a few more input such as the azimuth angular velocity target $\dot{\phi}_{Az}$, which sets the payload's slew speed in the gondola reference frame.

3.1 Gondola pointing stability with high bay doors closed

Before discussing the control system results, it is essential to clearly define the reference frames and coordinate systems used in BETTII, as shown in Fig. 12. The main reference frames are those of the star camera (subscript *sc*), the gyroscopes (subscript *g*, and the telescope (subscript *tel*). For simplicity, we consider that the gyroscope reference is identical to the gondola reference frame (no subscript).

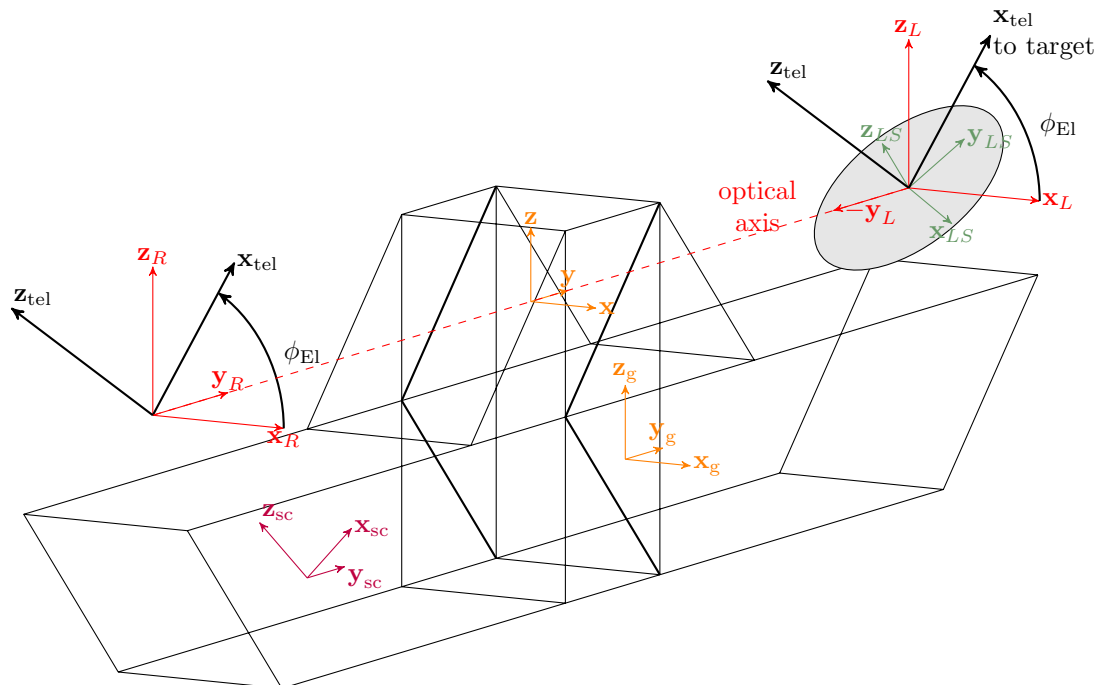


Figure 12: Coordinate systems relevant to the pointing control system (see text for details).

We routinely test the pointing stability indoors, without using the star camera. In this test the star camera is not functional and we do not have knowledge of the real RA and DEC of the payload.

When the payload is lifted and hangs uncontrolled, the motion about \mathbf{z} is shown in Fig. 13, and the power spectrum of the velocities is shown in Fig. 14a. The motion can be mostly characterized by an oscillation with a ~ 100 s period, which likely is caused by the restoring torque from the crane. The excitation is likely caused by the air conditioning of the high bay, as well as small motions of the high bay structure itself.

The PSD plots in Fig. 14a show that most of the motion occurs in \mathbf{z} at about 0.01 Hz. This motion is 3 orders of magnitude higher than any other contributor about \mathbf{z} . We can also notice a peak at 0.7 Hz that is visible in all axes, which we believe is an uncontrolled pitch motion of the payload about its long axis \mathbf{y} . Since we see the signature of this peak in all axes, this could indicate a misalignment of the gyroscopes within their mount or a non-diagonal inertia matrix of the payload. This can be caused for example by a pivot mode about the gondola attachment pin to the crane. The peak at 0.5 Hz is thought to be caused by a pivot mode about the same point but about the \mathbf{x} axis, which is the payload's short axis and has more inertia. The ratio of the two peak frequency roughly corresponds to the expected ratio of the moment of inertia about \mathbf{y} and \mathbf{x} . The peak at 0.15 Hz seen in both \mathbf{x} and \mathbf{y} is attributed to the pendulum mode about the crane attachment at the top of the building. This

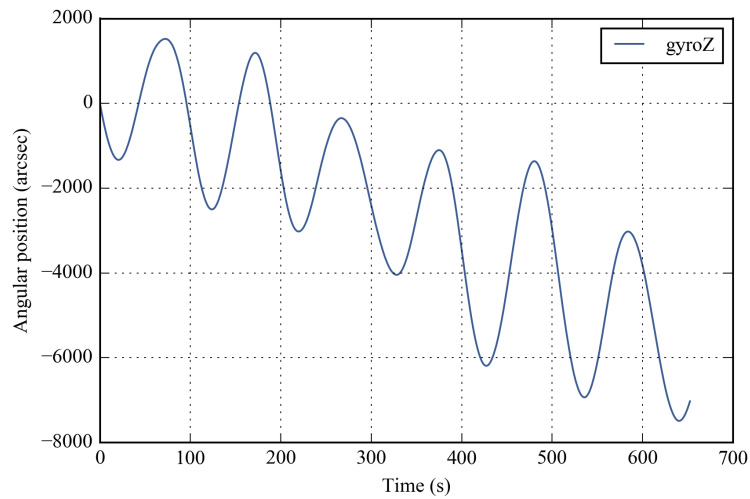


Figure 13: Integrated gyro time series while hanging and no motor on.

is consistent with a pendulum frequency $\frac{1}{2\pi}\sqrt{\frac{g}{L}}$ for $L \sim 20$ m. In flight, we expect that last mode to be at lower frequency, by at least a factor of $\sqrt{5}$, as the balloon train is expected to be at least 5 times longer.

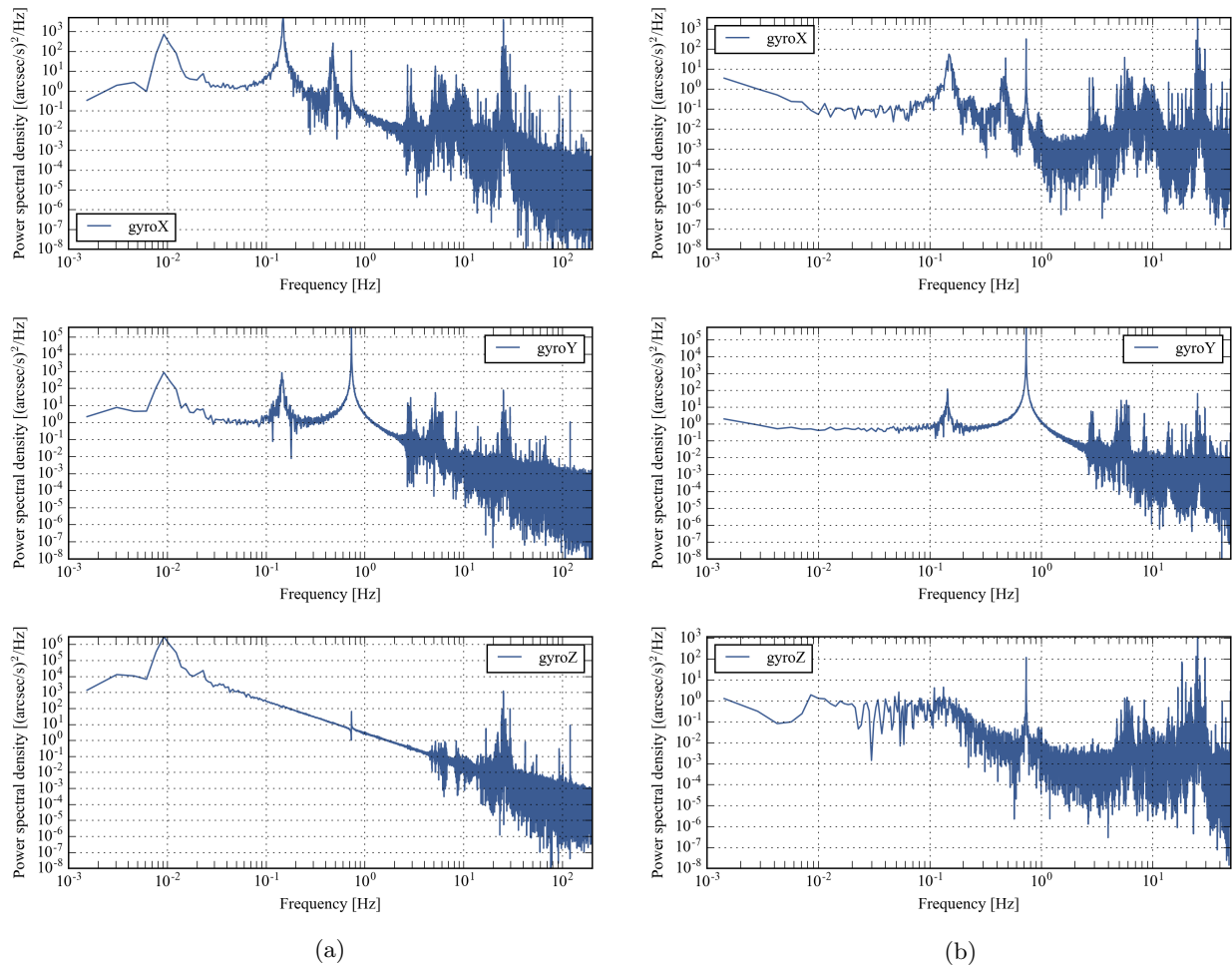


Figure 14: Noise while hanging indoors. (a) Uncontrolled lift. (b) Lift with controlled azimuth.

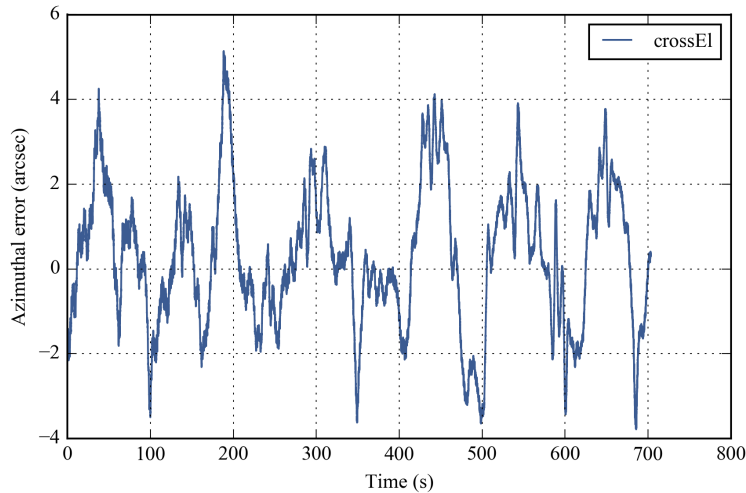


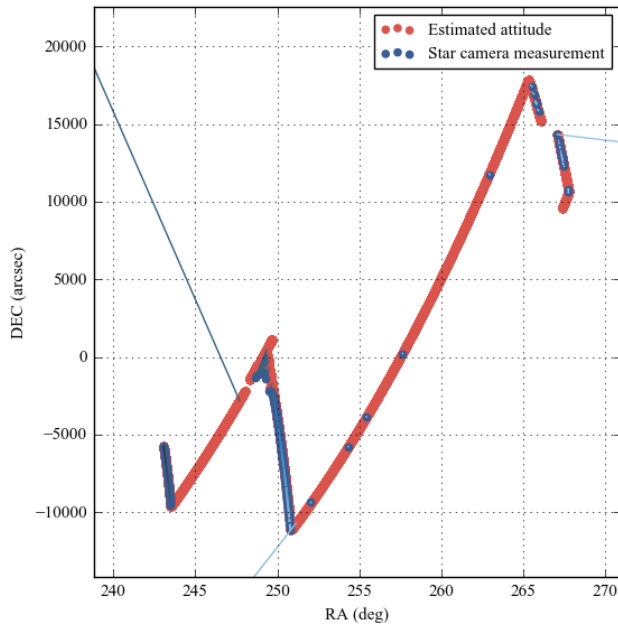
Figure 15: Cross-elevation error indoors.

Once lifted, the gyro PSD about \mathbf{z} is quite different (see Fig. 14b). We are indeed able to cancel out most of the drift by about 6 orders of magnitude in power at 0.01 Hz. The resulting time series showing the cross-elevation angle is shown in Fig. 15. The 1σ r.m.s noise of this 700 s run is $\leq 1''$. This reflects a 1000:1 rejection ratio when the control loop is on.

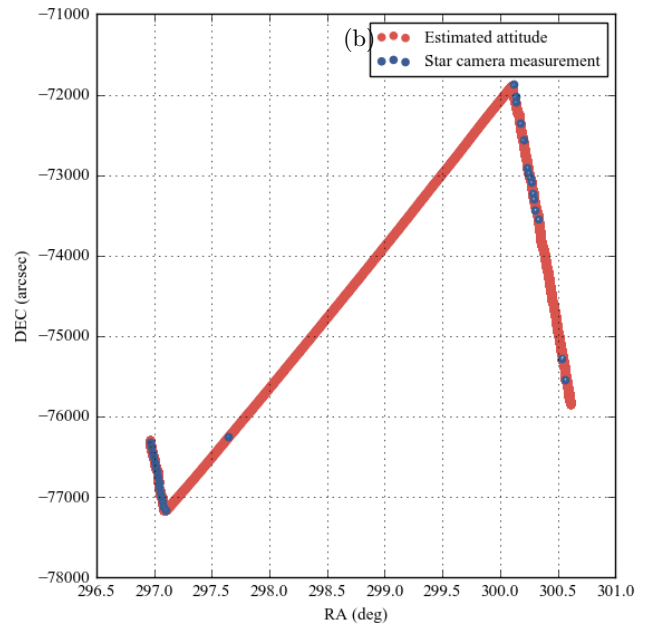
Note that this behavior also implies the momentum dump loop working well. While we do not have the data to show due a mistake in the archiving software, the CCMG gimbal angle was staying for all this time within a few degrees of zero, and has been working consistently well for multiple months before this writing. This has allowed us to always maintain the gimbal in the middle of the range, and ensured long-term stability.

3.2 On-sky pointing control

On-sky, lifted pointing test is the ultimate test that we can run from the ground without having the optics in place. We show two sets of data; the first one (configuration 1) was taken with the star camera positioned at $\sim 43^\circ$ elevation at the very end of the BETTII boom (pointing in the (\mathbf{y}, \mathbf{z}) plane). This gave access to a large patch of sky, as the boom could be almost sticking out through the high bay door. The second set (configuration 2) features the star camera installed at a temporary $\sim 23^\circ$ angle from horizontal in the (\mathbf{x}, \mathbf{z}) plane. This configuration is more similar to the final flight configuration where it will be at a nominal 45° from horizontal in that same plane. Putting it at an elevation of $\sim 23^\circ$ angle allows coverage of a reasonable patch of sky, although it remains very constraining.



(a)



(b)

Figure 16: Slew and point on the sky (a) Two consecutive slews with the camera in configuration 1 totalling ~ 25 deg in azimuth. The time flows from left to right on this graph. (b) Point, slew and point with the camera in configuration 2. The low rate of star camera solutions towards the end of the run is due to increased cloud coverage and increased surrounding light in the very early morning.

In Fig. 16 we show two typical pointing runs during a night in June 2016. That night marked the transition to configuration 2 and a reorganization of the high bay to accommodate rotating the payload so that it faces the door, and so that the telescopes can see out of the door.

For the first run that night, shown on Fig. 16a, we tested the new gyroscope mount, new algorithms, and new flight procedures. The run shows two consecutive slews (the swathes with little to no star camera solutions) spanning a total of about 25° in RA. Note that the scales are different in RA and DEC for display convenience. There are two noticeable features to this figure. The first is that some star camera solutions appear to be false positive, a result from non-optimal star camera parameters which involved too few stars required to confirm a match. This can be easily fixed by increasing this parameter.

The second, and more concerning problem is the apparent drift of the star camera solution after the first slew. This is what made us realize that correcting for biases only was not capturing the entire behavior of the gyroscope-star camera system pair. We interpret the resulting large error at the end of the first slew as a misalignment between the star camera orientation and the 3D gyroscope mount, and have developed flight software to properly estimate this out.

If this is a problem during flight, we anticipate resetting the estimator's position each time we finish slewing, to restart the Kalman filter using the original biases.

The second run of the night, which was also our first run in configuration 2, does not exhibit this behavior, partly due to a better alignment between the gyros and the star camera, and also because the slew is half as long as the first slew in the other picture.

For this second run, we show the pointing stability in cross-elevation in Fig. 17. This picture is to be compared with the test done indoors, showed in Fig. 15. Here the peak-to-peak errors are increased by a factor of ~ 5 , but the r.m.s deviation is still $\leq 5''$. This satisfies the $\pm 15''$ requirement for more than 95% of the points, which is very encouraging.

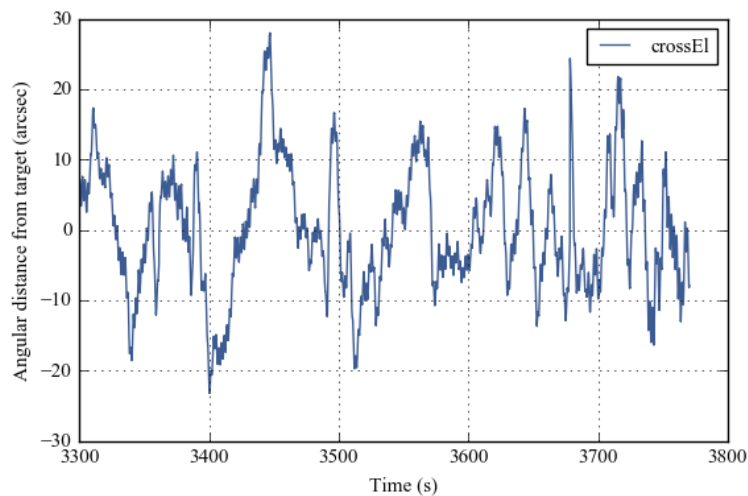


Figure 17: Cross-elevation error for a test on the sky (see text for description).

Another view at the pointing stability is proposed in Fig. 18, which presents the data as a 2D plot of the error in both elevation and cross-elevation, augmented by a 2D Kernel density contour plot to better show where the density peak lies. Note that contours are separated linearly, so that data is 10 times more likely to be inside the brightest contour than outside the black outer contour. The values of the contours are not meaningful, since they refer to lines of same probability density, which doesn't easily relate to a percentile value.

The striking asymmetry of this plot reveals that the elevation control is, for now, much more accurate than the cross-elevation loop, which is to be expected due to the much lower inertia of the rotators (at the time of

this run, the mirrors were not installed on the rotators). We expect degradation of the elevation accuracy once the siderostats are mounted on the rotators, even after tuning the PID gains.

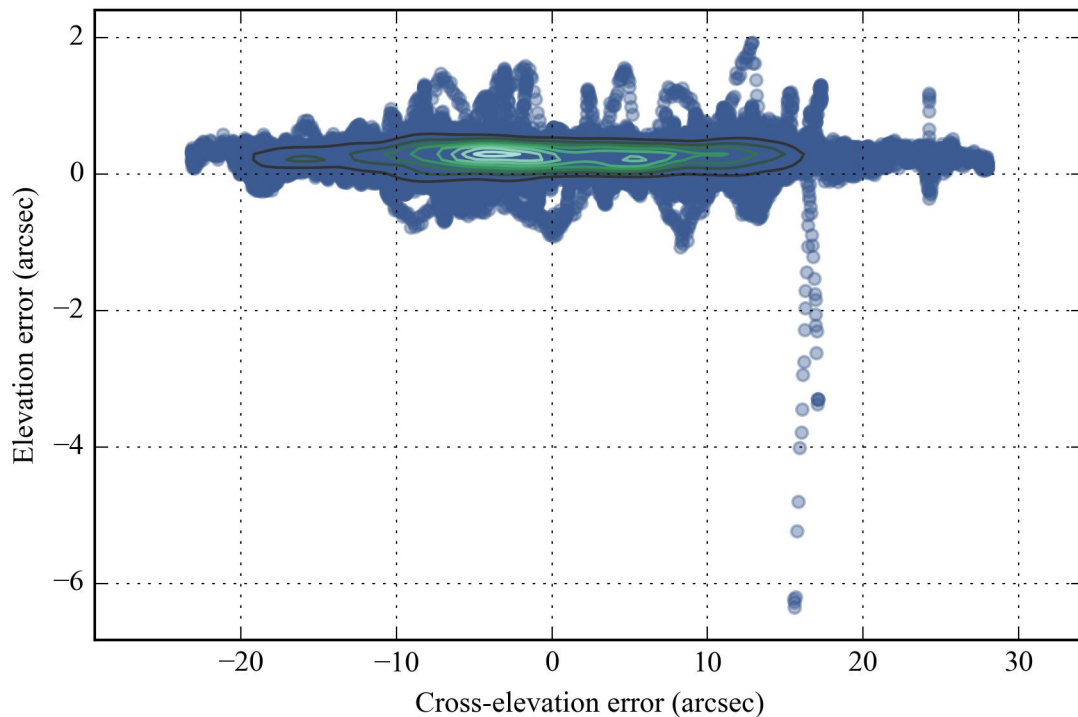


Figure 18: Elevation and cross-elevation error for a test on the sky.

3.3 Conclusion on coarse pointing

The last on-sky pointing tests have consistently shown:

1. our ability to always know where we are pointed using a robust star camera solution
2. our ability to slew large amounts while maintaining the wheels close to their zero position (which indicates a successful momentum dumping loop)
3. our ability to keep the telescope vector pointed to an inertial target to within the specified $\pm 15''$ for a large fraction of the time
4. our ability to have small attitude errors which can be fed to the delay line for further correction (not discussed in this paper).

These present key successes on our path for launch readiness. The last piece of the puzzle is to implement the fine guiding loop, which uses a NIR H1RG array to centroid a guide star. This last element will be implemented and tested in August 2016.

4. FLIGHT PLANNING

The primary science targets for BETTII have fluxes that are above the spectral sensitivities,⁷ with a bright NIR guide star nearby. In addition, in order to correctly know the OPD, we need sets of bright calibrator targets which provide periodic high-SNR fringes in one single scan of the delay line.

The science targets need to be available during our launch window, and preferably cover a large range of projected angles (so we can study the source at multiple angles to retrieve more of the spatial distribution). For this reason, we favor circumpolar sources, since they are the ones which change orientation at the fastest pace.

4.1 Calibrators

Calibrators ideally need to be point sources $\gg 100$ Jy in our FIR bands, and it is not straightforward to identify which astronomical sources exist that would provide this kind of flux density. The planets of our solar system and their moons are usually bright enough, but they are often resolved by our instrument, which dramatically reduce their interferometric contrast (see Fig. 19). For example, we estimate the Uranus is > 1000 Jy, but because it is resolved, the actual fringe contrast is very small, hence drastically reducing the SNR. Nearby, bright A stars such as Alpha Boo are most likely point sources, but are usually not as bright as we would want, especially not in Band 2 since they are essentially thermal sources with temperatures of thousands of Kelvin. It is possible to use actual science sources as calibrators, but of course it is unknown whether or not they actually are extended (this is the purpose of a mission like BETTII!).

We find that bright asteroids such as Ceres, Pallas and Vesta are the best candidates for bright calibrators (respectively $> 320, 150$ and 120 Jy). In addition, because of their albedo, they also reflect the sunlight so they would also be suitable for the tracking channels (e.g. Ceres has $H_{\text{mag}} \sim 3$). Their only disadvantage is that they are not inertial targets - this complicates the pointing control system as their expected position moves across the sky, which requires the payload to have accurate timing capabilities to know where the object is at a given time.

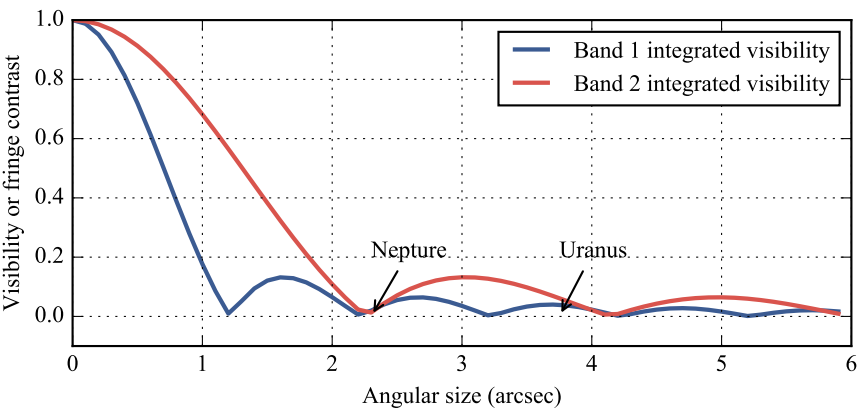


Figure 19: Visibilities of calibrators.

4.2 Science targets

Table 3: BETTII Targets		
Cluster	Coordinates	Fraction of night time between 15-75° elevation
S140	22h19m23s +63d18m44s	100.0 %
Cepheus A	22h56m10s +62d03m26s	100.0 %
NGC 7129	06h41m07s +09d33m35s	100.0 %
IRAS 20050+2720	20h07m05s +27d28m51s	50.0 %

The BETTII source list for the first flight is presented in Table 3, and includes the fraction of time that the target spends above 15 degrees elevation and below 75° during the planned observing night of September 15, 2016. In addition, Fig. 20 shows the tracks in the sky. The circumpolar targets S140, Cepheus A and NGC 7129 are available for the most time. All are located well in the East at the beginning of the night, which means we can point towards them as the Sun sets in the West. Note that when the source is at low elevations, we could experience a substantial amount of additional atmospheric noise since the line of sight sees more airmass.

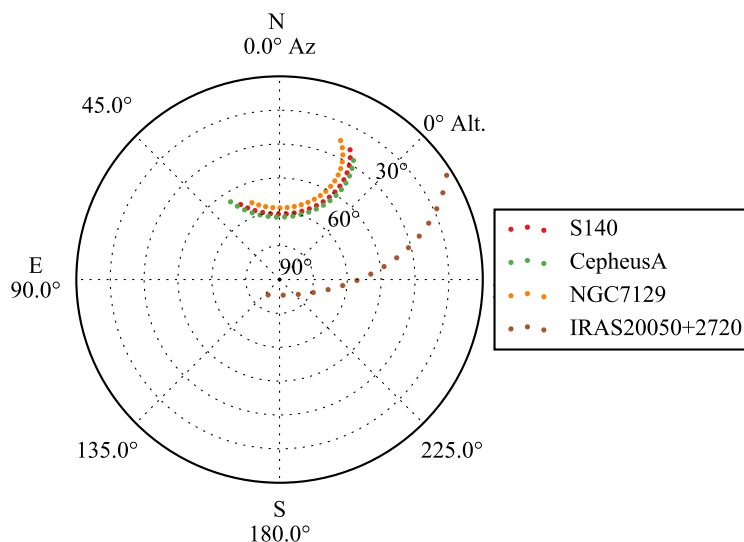


Figure 20: Polar plot showing the tracks of our targets in the night sky, between 8pm on Sept 15th and 6am on Sept 16th. The coordinates represent the local azimuth (with respect to North) and elevation, which is 0° at the horizon.

5. CONCLUSION

Significant progress has been achieved in getting the coarse pointing system of BETTII to flight readiness. In this paper we share results of our gyroscope and star camera characterization, and present the first integrated on-sky pointing test results. A consistent pointing control to within the requirement of $\pm 15''$ is achieved in the lab routinely. The last element of the pointing control system, the fine pointing loop is due to come online in August 2016 and be ready for intensive testing at the launch facility in Fort Sumner, NM. The BETTII sources for the first flight are briefly discussed.

ACKNOWLEDGMENTS

The material presented in this paper is based upon work supported by NASA Science Mission Directorate through the ROSES/APRA program, with additional support provided by NASA's Goddard Space Flight Center. Work by R. Juanola-Parramon and T. Veach was supported by an appointment to the NASA Postdoctoral Program at GSFC, administered by the Oak Ridge Associated Universities under contract with NASA. The BETTII program at Cardiff University and UCL is supported by an STFC PRD grant.

REFERENCES

- [1] Rinehart, S. A., Rizzo, M., Benford, D. J., Fixsen, D. J., Veach, T. J., Dhabal, A., Leisawitz, D. T., Mundy, L. G., Silverberg, R. F., Barry, R. K., Staguhn, J. G., Barclay, R., Mentzell, J. E., Griffin, M., Ade, P. A. R., Pascale, E., Klemencic, G., Savini, G., and Juanola-Parramon, R., “The Balloon Experimental Twin Telescope for Infrared Interferometry (BETTII): An Experiment for High Angular Resolution in the Far-Infrared,” *Publications of the Astronomical Society of the Pacific* **126**, 660–673 (July 2014).
- [2] Veach, T. J., Rinehart, S. A., Mentzell, J. E., Silverberg, R. F., Fixsen, D. J., Rizzo, M. J., Dhabal, A., Gibbons, C. E., and Benford, D. J., “The balloon experimental twin telescope for infrared interferometry (BETTII): optical design,” in [*Proceedings of the SPIE*], Rajagopal, J. K., Creech-Eakman, M. J., and Malbet, F., eds., 91462H–91462H–12, NASA Goddard Space Flight Ctr. (United States), International Society for Optics and Photonics (July 2014).
- [3] Rizzo, M. J., Rinehart, S. A., Alcorn, J. B., Barclay, R. B., Barry, R. K., Benford, D. J., Dhabal, A., Fixsen, D. J., Gore, A. S., Johnson-Shapoval, S., Leisawitz, D. T., Maher, S. F., Mundy, L. G., Papageorgiou, A., Pascale, E., Rau, A., Silverberg, R. F., Taraschi, P., Veach, T. J., and Weinreich, S., “Building an interferometer at the edge of space: pointing and phase control system for BETTII,” in [*Proceedings of the SPIE*], Oschmann, J. M., Clampin, M., Fazio, G. G., and MacEwen, H. A., eds., 91433H–91433H–12, Univ. of Maryland, College Park (United States), SPIE (Aug. 2014).
- [4] El Badaoui, N., Morbieu, B., Martin, P., Rouchon, P., Pocholle, J.-P., Guty, F., Feugnet, G., and Schwartz, S., “Towards a solid-state ring laser gyroscope,” *Comptes Rendus Physique* **15**, 841–850 (Dec. 2014).
- [5] Peltier, J., [*Investigation of the heat developed by electric currents in homogeneous materials and at the junction of two different conductors*], Ann. Chim. Phys (1834).
- [6] Oxley, P., Ade, P. A., Baccigalupi, C., deBernardis, P., Cho, H.-M., Devlin, M. J., Hanany, S., Johnson, B. R., Jones, T., Lee, A. T., Matsumura, T., Miller, A. D., Milligan, M., Renbarger, T., Spieler, H. G., Stompor, R., Tucker, G. S., and Zaldarriaga, M., “The EBEX experiment,” *Infrared Spaceborne Remote Sensing XII. Edited by Strojnik* **5543**, 320–331 (Nov. 2004).
- [7] Rizzo, M. J., Mundy, L. G., Dhabal, A., Fixsen, D. J., Rinehart, S. A., Benford, D. J., Leisawitz, D., Silverberg, R., Veach, T., and Juanola-Parramon, R., “Far-Infrared Double-Fourier Interferometers and their Spectral Sensitivity,” *Publications of the Astronomical Society of Pacific* **127**, 1045–1060 (Oct. 2015).